Astronomy
&
Astrophysics

SN 2024ggi: Another year, another striking Type II supernova

K. Ertini[1,2,★] , T. A. Regna[1,2] , L. Ferrari[1,2] , M. C. Bersten[1,2,3] , G. Folatelli[1,2,3], A. Mendez Llorca[1,2] ,
E. Fernández-Lajús[1] , G. A. Ferrero[2,1] , E. Hueichapán Díaz[4,5] , R. Cartier[4] , L. M. Román Aguilar[1,2] ,
C. Putkuri[1] , M. P. Piccirilli[2,6] , S. A. Cellone[7,2] , J. Moreno[1,2] , M. Orellana[8,6] , J. L. Prieto[4,5],
M. Gerlach[4,5,9] , V. Acosta[2], M. J. Ritacco[2], J. C. Schujman[2], and J. Valdéz[2]

[1] Instituto de Astrofísica de La Plata (IALP), CCT-CONICET-UNLP, Paseo del Bosque, B1900FWA La Plata, Argentina
[2] Facultad de Ciencias Astronómicas y Geofísicas, Universidad Nacional de La Plata, Paseo del Bosque S/N, 1900 La Plata, Buenos Aires, Argentina
[3] Kavli Institute for the Physics and Mathematics of the Universe (WPI), The University of Tokyo, 5-1-5 Kashiwanoha, Kashiwa, Chiba 277-8583, Japan
[4] Instituto de Estudios Astrofísicos, Facultad de Ingeniería y Ciencias, Universidad Diego Portales, Av. Ejército Libertador 441, Santiago, Chile
[5] Millennium Institute of Astrophysics MAS, Nuncio Monseñor Sotero Sanz 100, Off. 104, Providencia, Santiago, Chile
[6] Consejo Nacional de Investigaciones Científicas y Técnicas (CONICET), Godoy Cruz 2290, 1425 Ciudad Autónoma de Buenos Aires, Argentina
[7] Complejo Astronómico El Leoncito (CASLEO), CONICET – UNLP – UNC – UNSJ, Av. España 1512 (sur), J5402DSP San Juan, Argentina
[8] Universidad Nacional de Río Negro. Sede Andina, Laboratorio de Investigación Científica en Astronomía, Anasagasti 1463, Bariloche (8400), Argentina
[9] Instituto de Astrofísica, Facultad de Física, Pontificia Universidad Católica de Chile, Av. Vicuña Mackenna 4860, Santiago, Chile

ABSTRACT

Context. SN 2024ggi is a Type II supernova that exploded in the nearby galaxy NGC 3621 at a distance of approximately 7 Mpc, making it one of the closest supernovae of the decade. It shows clear signs of interaction with a dense circumstellar material (CSM), and several studies have investigated the properties of its possible progenitor star using pre-explosion data.

Aims. We aim to constrain the progenitor properties of SN 2024ggi by performing hydrodynamical modelling of its bolometric light curve and expansion velocities using our own spectrophotometric data.

Methods. We present photometric and spectroscopic observations of SN 2024ggi obtained with the Complejo Astronómico El Leoncito, with Las Campanas Observatory, and with Las Cumbres Observatory Global Telescope Network spanning from 2 to 106 days after explosion. We constructed its bolometric light curve and characterised it by calculating its morphological parameters. Then, we computed a grid of one-dimensional explosion models for evolved stars with varying masses and estimated the properties of the progenitor star of SN 2024ggi by comparing the models to the observations.

Results. The observed bolometric luminosity and expansion velocities are well matched by a model that includes the explosion of a star in the presence of a close CSM, with a zero-age main sequence mass of $M_{ZAMS} = 15\,M_\odot$, a pre-supernova mass and radius of $14.1\,M_\odot$ and $517\,R_\odot$, respectively, an explosion energy of 1.2×10^{51} erg, and a nickel mass below $0.035\,M_\odot$. Models of $M_{ZAMS} = 13\,M_\odot$ and $18\,M_\odot$ were unable to reproduce the observations. Our analysis suggests that the progenitor suffered a mass-loss rate of $4 \times 10^{-3}\,M_\odot\,yr^{-1}$ within a radius of $3000\,R_\odot$. The CSM distribution is likely a two-component structure that consists of a compact core and an extended tail. This analysis represents the first hydrodynamical model of SN 2024ggi with a complete coverage of the plateau phase.

Key words. stars: massive – supernovae: general – supernovae: individual: SN 2024ggi

1. Introduction

Type II supernovae (SNe II) mark the end of the life of massive stars ($\gtrsim 8\,M_\odot$) that have retained their hydrogen envelopes. A subclass of SNe II are Type IIn SNe, which show narrow lines in the spectra that come from the ejecta colliding with circumstellar material (CSM; Schlegel 1990). In the last decade, observations of some SNe II revealed early spectra showing narrow lines of highly ionised material, typical of IIn SNe; these lines disappear hours to days later, and the SNe thus become 'normal' (Yaron et al. 2017). With modern high-cadence sur-

veys discovering younger SNe just a few hours after their first light, these types of observations have became increasingly common. Bruch et al. (2023) analysed a sample of 40 SNe II with good early spectral coverage (spectra obtained within $\lesssim 2$ days of the explosion epoch) and find that 40% showed flash ionised features, suggesting that this is a rather common phenomenon. Modelling of the SNe that show flash features suggests that their red supergiant (RSG) progenitors ejected material at an unexpectedly high mass-loss rate prior to the explosion (Yaron et al. 2017; Dessart et al. 2016).

In 2023, the Type II SN 2023ixf (Perley et al. 2023) was discovered in the M101 galaxy (Itagaki 2023). Its proximity and early detection made it possible to obtain a vast amount

---

of observations across multiple wavelengths. In particular, flash spectra were taken less than a day after the discovery: they showed narrow features of H I, He I/II, C IV, and N III/IV/V, a sign of interaction with a dense CSM (Jacobson-Galán et al. 2023). In addition, SN 2023ixf was an excellent opportunity to study the environment and progenitor system of a type II SN in detail. Pre-explosion observations of the SN 2023ixf site suggest a dusty RSG progenitor, with zero-age main sequence (ZAMS) mass estimates ranging from 8 to 18 $M_\odot$ (Qin et al. 2024; Kilpatrick et al. 2023; Jencson et al. 2023; Xiang et al. 2024; Neustadt et al. 2024; Van Dyk et al. 2024). Mass estimates based on additional methods, such as variability studies of the pre-SN source, stellar population analyses, hydrodynamical modelling, and nebular spectroscopy, increased the estimated ZAMS mass range to 8–22 $M_\odot$ (Soraisam et al. 2023; Niu et al. 2023; Liu et al. 2023; Bersten et al. 2024; Ferrari et al. 2024).

Another very nearby Type II SN, SN 2024ggi, was discovered by the Asteroid Terrestrial-impact Last Alert System (ATLAS; Tonry et al. 2018) on 11 April 2024 (MJD = 60411.14) with a magnitude of 18.92 ± 0.08 in the ATLAS o band (Srivastav et al. 2024; Chen et al. 2025). The host galaxy of SN 2024ggi is NGC 3621, which is located at a distance of 6.7 Mpc (Paturel et al. 2002). It was spectroscopically classified by Zhai et al. (2024), and its last published non-detection was by Killestein et al. (2024) on MJD = 60410.45, i.e. only 0.69 days before the detection. A spectrum taken the day of the discovery revealed flash ionised features (Hoogendam et al. 2024). Since then, comprehensive ultraviolet and optical photometry, as well as spectroscopy, was obtained with high cadence (Jacobson-Galán et al. 2024; Pessi et al. 2024; Chen et al. 2024; Shrestha et al. 2024). Follow-up observations across other wavelengths were also triggered, including detections in X-rays (Zhang et al. 2024a; Margutti & Grefenstette 2024; Lutovinov et al. 2024) at 2.4, 2.5, and 3 days post-explosion and in radio (Ryder et al. 2024) three weeks after the explosion. Additionally, non-detections were reported in the centimetre and millimetre regimes (Chandra et al. 2024; Hu et al. 2025) and in γ-rays (Marti-Devesa & Fermi-LAT Collaboration 2024). Flash spectra were studied in detail by Jacobson-Galán et al. (2024), Pessi et al. (2024), and Shrestha et al. (2024). Just hours after the discovery, emission lines of the Balmer series, He I, C III, and N III were detected, and less than a day after that emission lines of He II, C IV, N IV/V, and O V became visible. This increase in ionisation was accompanied by an evolution towards bluer colours. The duration of the flash features was 3.8 ± 1.6 days (Jacobson-Galán et al. 2024).

Given its proximity, SN 2024ggi offers yet another valuable opportunity to probe the progenitors of Type II SNe. Shortly after its discovery, several telegrams reported searches of its progenitor in archival data. Komura et al. (2024) examined *XMM-Newton* archival observations for X-ray emission but identified no apparent X-ray source at the SN position. Additionally, Srivastav et al. (2024) and Yang et al. (2024) reported a possible red progenitor source in archival data from the Legacy Survey and *Hubble* Space Telescope (HST), and Pérez-Fournon et al. (2024) identified a likely progenitor in near-IR archival imaging and catalogues of the VISTA Hemisphere Survey.

Following these telegrams, further studies analysed archival data to investigate the progenitor. Using pre-explosion images from the HST and the *Spitzer* Space Telescope, Xiang et al. (2024) inferred that the progenitor of SN 2024ggi was a red bright variable star with a pulsational period of approximately 379 days in the mid-IR. By fitting the progenitor's spectral energy distribution, they derived an initial mass of 13 $M_\odot$. Additionally, Chen et al. (2024), based on archival deep images from the Dark Energy Camera Legacy Survey, suggested a possible progenitor with an initial mass in the range 14−17 $M_\odot$.

Independently of direct progenitor detections, Hong et al. (2024) performed an environmental analysis based on images from the HST. From the age of the youngest stellar population in the environment of the SN that is associated with the progenitor, they derived for the SN an initial mass of 10.2 $M_\odot$.

In this study we adopted an alternative approach to estimating the progenitor mass of SN 2024ggi, by comparing hydrodynamical explosion models with the bolometric light curve (LC) and expansion velocity evolution of the SN. This work represents the first attempt to do so using data covering the full extent of the plateau phase. Additionally, we present photometric and spectroscopic follow-up of SN 2024ggi starting 5 days after the explosion.

In Sect. 2 we present the observations and data reduction of SN 2024ggi. We analyse its photometric and spectroscopic properties, as well as its bolometric LC, in Sect. 3, and in Sect. 4 we present the associated hydrodynamical modelling for the proposed progenitor scenario. In Sect. 5 we provide a summary of our results.

2. Data sample

We obtained direct images with the 60 cm *Helen Sawyer Hogg* (HSH) telescope at the Complejo Astronómico El Leoncito (CASLEO), located in San Juan, Argentina, through the programmes HSH-2024A-DD01 (PI Ertini) and HSH-2024A-02 (PI Fernández-Lajús). The observations were obtained with a nearly daily cadence, from 5 to 35 days post explosion. We used the B, V, R, and I filters. The observations were divided into ten exposures of 40 seconds each for VRI bands and 60 seconds each for the B band. Sky flats were taken each day of observation. The reduction was performed following standard procedures in Python. The photometry was performed using the software AutoPhOT (Brennan & Fraser 2022). The software determines whether to utilise aperture or point-spread function (PSF) photometry. It starts with aperture photometry as an initial estimate to determine the approximate magnitude of the SN, then attempts to apply PSF photometry. By default, the source must have a signal-to-noise ratio greater than 25 to be considered for the PSF model. If PSF fitting is not feasible, aperture photometry is used instead. The instrumental magnitudes are then calibrated to the standard system estimating a zero point, which is calculated using ~20 field stars from the Panoramic Survey Telescope and Rapid Response System (Pan-STARRS; Flewelling et al. 2020). Since the Pan-STARRS magnitudes are in gri we first used the transformation coefficients of Tonry et al. (2018) to transform the magnitudes of the field stars into $BVRI$. The photometry is listed in Table A.1.

We also obtained images using the 1 m telescope of Las Cumbres Observatory Global Telescope Network (LCOGTN) located at Cerro Tololo. These observations were conducted from 2 to 85 days post-explosion, with a typical cadence of one observation approximately every three days. There was 12-day gap in coverage due to adverse weather conditions. Additionally, a final observation was taken 106 days after the explosion. The reduction of LCOGTN data was done by using a new python version of the custom Image Reduction and Analysis Facility (IRAF; Tody 1986) script package described in Hamuy et al. (2006) and Contreras et al. (2010). LCOGT photometry is listed in Table A.2.

Table 1. Spectroscopic observations.

Date	MJD	Telescope	Instrument	Phase
2024 Apr 16	60416.05	JS	REOSC	5.3
2024 Apr 23	60423.98	JS	REOSC	13.2
2024 Apr 24	60424.97	JS	REOSC	14.2
2024 Apr 25	60425.98	JS	REOSC	15.2
2024 May 01	60431.21	JS	REOSC	20.4
2024 Jul 03	60494.90	Clay	LDSS-3	83.9

Notes. The phase is indicated in rest-frame days from explosion.

Spectra were acquired with the REOSC spectrograph mounted on the 2.15 m *Jorge Sahade* (JS) telescope (programme JS-2024A-DD01, PI Ertini) at CASLEO. We used the 200-mic slit and the #270 grating, covering a wavelength range of 3400–7600 Å. The data reduction included wavelength and flux calibration using arc lamps and spectrophotometric standard stars, respectively. The spectral resolution measured from skylines in the spectra is ≈ 8 Å, which results in ≈ 480 km s^{-1} at 5000 Å. We also obtained one spectrum using the LDSS-3 spectrograph mounted at the 6.5 m Magellan Clay telescope at Las Campanas Observatory on July 3, 2024 at 23:18:40 UT (MJD = 60494.97). The SN was observed at the parallactic angle using the 1″ slit width in combination with the VPH-ALL 400 lines/mm grism providing a resolution of 8.2 Å (R = 900), and covering a wavelength range of 4250–10 000 Å. A HeArNe comparison lamp was obtained immediately after the SN spectrum to perform the wavelength calibration. The spectrum was reduced and flux calibrated using IRAF routines (see Cartier et al. 2024). The log of spectroscopic observations is listed in Table 1.

3. Observational properties

We took the explosion epoch as the midpoint between the last non-detection and the first detection with an uncertainty equal to half the interval between those epochs, at MJD = 60410.795 ± 0.345. We adopted the redshift given by Koribalski et al. (2004) of 0.0024 to correct the spectra and the LC phases.

3.1. Light curves and colour evolution

The *BVRI* and *griz* LCs are presented in Fig. 1. The photometry from LCOGTN has been transformed from AB to Vega photometric system for a better display. Table A.2 shows the original measurements in the AB system. We fitted the LCs corrected by extinction (see Sect. 3.3) using a low-order polynomial in order to get peak magnitudes and rise times. This was done only on *griz* since these bands are better sampled and have enough coverage during the rise. The results are listed in Table 2. We obtained an absolute peak magnitude in the *r* band of $M_r = -17.73$ mag at MJD = 60419.63, giving a rise time of $t_r = 8.8$ days. The uncertainty in the absolute peak magnitude is the result of adding in quadrature the fitting error, the uncertainty in the peak phase, and the uncertainty in the distance. The uncertainty in the rise time is taken as the uncertainty in the explosion epoch, since it is the main source of error.

The rise times are longer the redder the band is, indicating that the peak is due to a decrease in temperature, corresponding to the well-known cooling phase prior to the recombination of
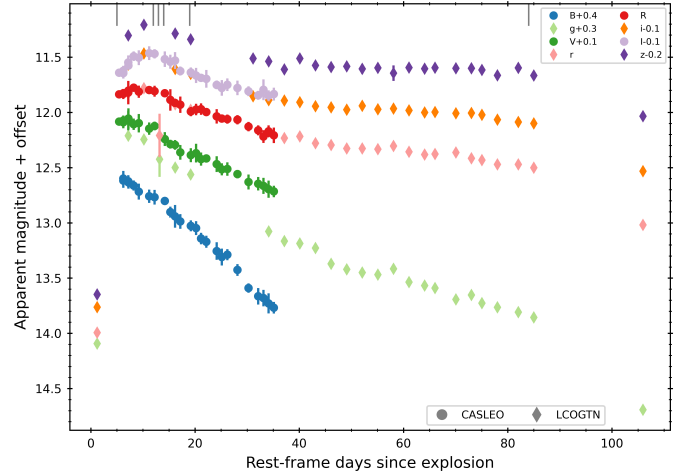

Fig. 1. Observed LCs of SN 2024ggi. For clarity, the LCs are shifted by the offsets indicated in the upper legend. Different instruments are indicated with different markers. Rest-frame epochs of optical spectra are marked as grey lines along the top axis.

Table 2. LC properties of SN 2024ggi.

Filter	MJD$_{max}$	$t_{rise}^{(a)}$ [days]	M_{max} [mag]
g	60418.00	7.2	-17.87 ± 0.02
r	60419.63	8.8	-17.73 ± 0.01
i	60422.93	12.14	-17.84 ± 0.01
z	60422.70	11.9	-17.40 ± 0.01

Notes. $^{(a)}$ The uncertainty in the rise times is set to 0.3 days, corresponding to the uncertainty in the explosion epoch, which is the dominant source of error.

SNe II. The plateau lasts around 90 days in *r*, *i*, and *z* bands, while there is a minor decline in the *g* band.

3.2. Spectral properties

The spectroscopic data of SN 2024ggi that cover the phases from 5 to 84 days after the explosion are presented in Fig. 2 and compared with the standard Type II plateau SN 1999em. The rest-wavelength positions of the main features are marked with dashed lines. Our spectra cover the interval between 5 and 20 days well, and then there is a gap until 84 days. During the evolution, the continuum becomes less blue with time, consistent with the colour evolution derived from the LCs. As noted by Jacobson-Galán et al. (2024) and Shrestha et al. (2024), in the spectrum at five days after explosion, which is our first spectrum, there is no evidence of high ionisation lines. In the first spectrum, weak, broad absorption features of Hβ, He I λ 4471, and He I λ 5876 are present. The SN evolves slowly during the first 20 days, developing typical P-Cygni profiles. At 13 days, the Hα and Fe II λ 5169 profiles are clearly visible. The velocity of the Hα line, measured from the absorption minimum, goes from ≈ -9500 to ≈ -9000 km s^{-1} between 5 and 20 days, while Fe II λ 5169 velocity varies from ≈ -7800 to ≈ -6900 km s^{-1} between 13 and 20 days.

The spectra of SN 2024ggi matches those of typical SNe II, as noticed by the comparison with SN 1999em. However, during the first 20 days of its evolution, the Hα absorption is weaker and less pronounced than that observed in SN 1999em. This weak Hα profile may be associated with the presence of an ejecta–CSM

interaction ([Hillier & Dessart 2019](#)) and is generally linked to brighter and more rapidly declining SNe II ([Gutiérrez et al. 2014](#)). Between 13 and 20 days, the spectra of SN 2024ggi exhibit the 'Cachito' feature, an absorption component on the blue side of Hα ([Gutiérrez et al. 2017](#)), which is also seen in the 21-day spectrum of SN 1999em. For SN 1999em, this feature had been proposed to be due to high velocity structures in the expanding ejecta of the SN ([Baron et al. 2000](#); [Leonard et al. 2002](#)). Since then, it is been identified in different SNe as either high velocity Hα or Si II 6355 Å ([Pastorello et al. 2006](#)). If this feature is high-velocity Hα, it would be associated with the interaction between the ejecta and CSM ([Chugai et al. 2007](#)). [Gutiérrez et al. (2014)](#) proposed that when Cachito is detected within 30 days post-explosion, it is more likely to be associated with Si II, whereas detections at later epochs are linked to high-velocity Hα. Since the Cachito feature in SN2024ggi is observed within this early time frame, it is likely associated with Si II.

At 84 days, the SN has evolved considerably, decreasing its blue continuum and developing features corresponding to Fe II, Sc II, H, and O I. The Hα profile becomes strong, followed by the calcium near-IR triplet feature. This last spectrum covers the wavelength range beyond 7200 Å and until 9700 Å. At this phase, the Hα absorption has shifted to $\approx -5900 \, \mathrm{km \, s^{-1}}$, and the Fe II λ 5169 to $\approx -3200 \, \mathrm{km \, s^{-1}}$. All the features described here are marked in Fig. 2. Note that at 84 days, the Cachito feature had disappeared.

3.3. Bolometric evolution

We first calculated the bolometric luminosity of SN 2024ggi. To have accurate constraints on the CSM properties, early observations are needed. Our dataset spans from 5 days to 35 days from explosion in *BVRI* and from 2 to 106 in *griz*. Since we only made one observation in the first 5 days after explosion, which are crucial to determine the CSM properties, we added high cadence early photometry of SN 2024ggi published by [Shrestha et al. (2024)](#) to our observations. This dataset is composed by ultraviolet (UV) and optical observations in the filters *UVW2*, *UVM2*, *UVW1*, *U*, *B*, *g*, *V*, *r*, and *i*, from the first day until 21 days after explosion.

Although the observations are heavily sampled, magnitude values are sometimes missing for certain filters at a given epoch. To have the LCs with the same cadence across all filters, we linearly interpolated them. The gap between consecutive epochs to interpolate was always less than 2.5 days.

The next step is to correct the observed magnitudes by extinction. Regarding the Milky Way (MW) extinction, the recalibrated dust maps of [Schlegel et al. (1998)](#) yield a value of $E(B - V)_{\mathrm{MW}} = 0.07$ mag ([Schlafly & Finkbeiner 2011](#)) from the NASA Extragalactic Database (NED[1]), considering an extinction law from [Cardelli et al. (1989)](#) with $R_V = 3.1$. [Pessi et al. (2024)](#) find three intervening galactic clouds in the line of sight to the SN using high-resolution spectroscopy, inferring a total extinction of $E(B - V)_{\mathrm{MW}} = 0.12 \pm 0.02$ mag. This value does not compare well with the extinction from the recalibrated maps of [Schlafly & Finkbeiner (2011)](#). As noted by [Pessi et al. (2024)](#), the dust extinction map of [Schlegel et al. (1998)](#) is less accurate when multiple dust clouds with different temperatures are encountered, which may explain the discrepancy. Additionally, several estimates have been made for the host galaxy component of the extinction for this SN. [Jacobson-Galán et al. (2024)](#) inferred an $E(B - V)_{\mathrm{host}} = 0.084 \pm 0.018$ mag by calculating the
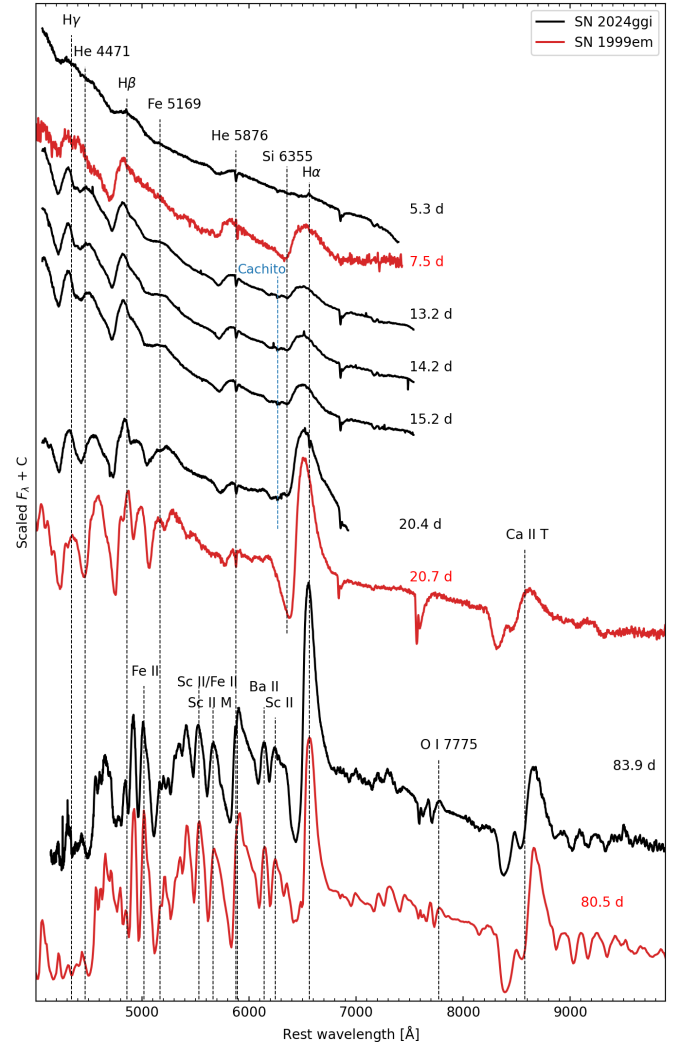
---

[1] https://ned.ipac.caltech.edu/

Fig. 2. Spectral sequence of SN 2024ggi taken with the JS and Magellan Clay telescopes, marked in black. Main absorption lines are marked with dashed lines at the rest wavelength. Spectra of SN 1999em are shown for comparison in red; epochs are referred to the explosion date derived by [Elmhamdi et al. (2003)](#).

Na I D1 and D2 equivalent widths from high resolution spectra, and using the calibrations from [Stritzinger et al. (2018)](#). Similarly, [Pessi et al. (2024)](#) calculated the host extinction to be $E(B - V)_{\mathrm{host}} = 0.036 \pm 0.007$ mag, and [Shrestha et al. (2024)](#) measured $E(B - V)_{\mathrm{host}} = 0.034 \pm 0.020$ mag, both using the calibrations from [Poznanski et al. (2012)](#). In summary, [Jacobson-Galán et al. (2024)](#), [Pessi et al. (2024)](#), and [Shrestha et al. (2024)](#) calculate a total $E(B - V)_{\mathrm{tot}}$ of 0.154, 0.16, and 0.154 mag respectively. We assumed $E(B - V)_{\mathrm{tot}} = 0.16$ mag.

After correcting the interpolated LCs by extinction, we converted them to monochromatic fluxes at the effective wavelength of each band. Then, we integrated the monochromatic fluxes along wavelength for each epoch, obtaining the quasi-bolometric flux (F_{qbol}). To account for the flux outside the observed wavelength range, we assumed that at early epochs, the SN emission is well represented by a blackbody (BB) distribution. We then extrapolated the UV and IR to obtain the unobserved UV and IR flux (F_{UV} and F_{IR}, respectively), by fitting a BB to the spectral energy distributions at each epoch. Blackbody fits were restricted to observational epochs with at least four bands, whether observed or interpolated. Then, the total bolometric flux
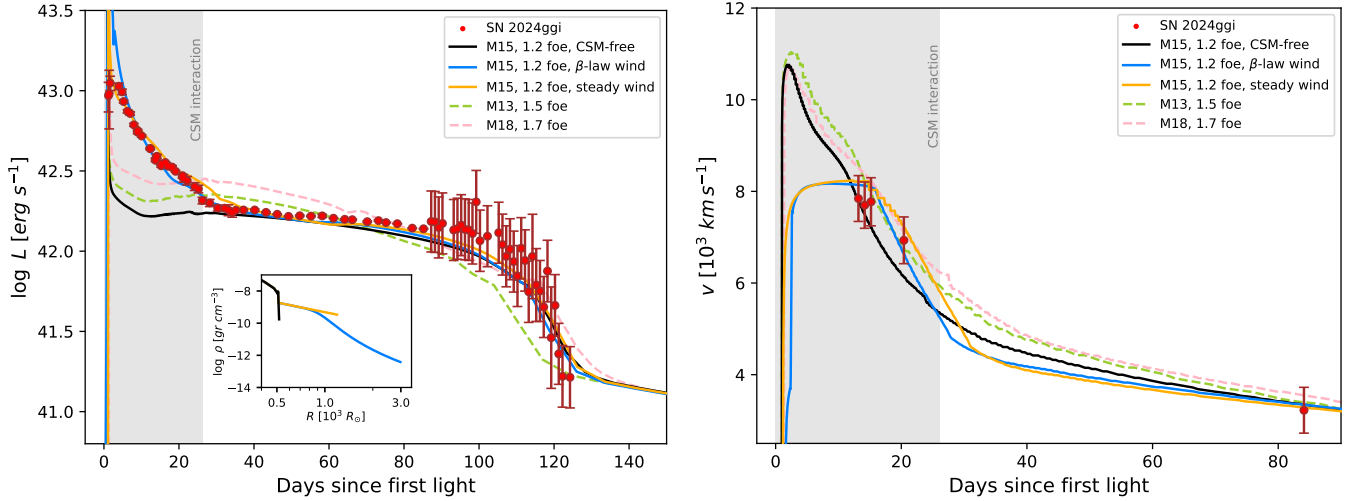
Fig. 3. Observations of SN 2024ggi (points) compared with hydrodynamical models (lines). Left panel: Bolometric LC. The inset shows density profiles of the models with no CSM (black), with a steady wind (yellow), and with an accelerated wind (blue). Right panel: Photospheric velocity evolution. The shaded grey area marks the approximate time frame during which the emission is dominated mainly by CSM interaction, i.e. times $t \lesssim Cd = 26$ d. The uncertainty on the velocities is taken as $\approx -500\,\mathrm{km\,s^{-1}}$, and this takes the resolution of the spectra and the error in the measurements into account.

was calculated as $F_{\mathrm{bol}} = F_{\mathrm{UV}} + F_{\mathrm{qbol}} + F_{\mathrm{IR}}$, and converted to luminosity assuming the distance stated in the introduction. The uncertainty in the luminosity was estimated by considering uncertainties in the photometry, distance, and the estimated errors of the extrapolated fluxes.

Our high-cadence data extend up to ~85 days post-explosion, then there is a 12 day gap before our last observation at 106 days post-explosion. Since this gap is too long to extrapolate, to calculate the bolometric LC beyond 85 days we used public photometry available in the B and V bands from the American Association of Variable Star Observers (AAVSO) web page[2] (Kloppenborg 2024). Around ~250 photometric measurements in the B band and ~400 in the V band are available contributed by different observers globally for SN 2024ggi, covering 125 days of the SN evolution. We adopted the mean magnitudes in daily bins after rejecting discrepant observations, beginning from 85 days post-explosion where our original data concluded. We corrected the magnitudes by extinction, and then we used the (B-V) colour-based bolometric corrections from Martinez et al. (2022a) to derive the bolometric magnitudes. The bolometric luminosities were then calculated using the distance adopted in the introduction. The uncertainties were calculated considering uncertainties in the photometry and in the bolometric corrections.

The complete bolometric LC is shown in Fig. 3. We determined the bolometric magnitude at maximum to be $M_{\mathrm{max}} = -18.920 \pm 0.001$ mag, and calculated the morphological bolometric LC parameters as defined by Martinez et al. (2022a, see their Fig. 8 and Anderson et al. 2014). These parameters essentially characterise the bolometric magnitudes in different parts of the LC, decline rates, and duration of the different phases. In summary each parameter is defined as follows: $s1$, $s2$, and $s3$ are the decline rates in magnitudes per 100 days during the cooling phase, the plateau phase, and the radioactive tail phase, respectively. The parameter t_{trans} corresponds to the epoch of transition between the cooling decline and the plateau decline. $optd$, p_d, and C_d correspond to the duration of the optically thick, plateau, and cooling phases, respectively. Finally, $M_{\mathrm{bol,end}}$ and

Table 3. Bolometric LC parameters of SN 2024ggi.

Parameter	SN 2024ggi	SN 2023ixf	CSP-I
$M_{\mathrm{bol,end}}$ [mag]	$-16.68(0.001)$	$-17.18(0.06)$	$-16.2(0.6)$
s_1 [mag/100 d]	7.12(0.10)	5.53(0.91)	4.59(2.84)
s_2 [mag/100 d]	0.55(0.02)	1.84(0.56)	0.81(0.91)
C_d [d]	26.21(1.75)	29.66(5.31)	26.9(4.3)
p_d [d]	93.23(1.41)	53.42(5.23)	75.0(26.2)
$optd$ [d]	119.44(0.34)	83.08(0.08)	104.3(19.3)

$M_{\mathrm{bol,tail}}$ are the bolometric magnitudes measured 30 days before and after t_{PT}, respectively, where t_{PT} is equivalent to $optd$. Due to the lack of data during the radioactive tail phase at the time of these calculations, we did not include values for M_{tail} or the s_3 decline rate. The results are listed on Table 3, together with the comparison of the same parameters for SN 2023ixf from Bersten et al. (2024). Additionally, we include in Table 3 the parameters calculated by Martinez et al. (2022a) using a large sample of SNe II from the Carnegie Supernova Project-I (CSP-I; Hamuy et al. 2006).

We find that most parameters of SN 2024ggi, similar to SN 2023ixf, fall within 1σ of the comparison distributions, suggesting it is a typical SN II. However, we note some minor deviations: SN 2024ggi exhibits a longer plateau duration and declines faster in the cooling phase than average, contrary to which was obtained for SN 2023ixf, which exhibited a shorter plateau duration, compared to the distribution of SNe II. A longer plateau duration suggests a more massive progenitor than the bulk of SNe II (Martinez et al. 2022b, see also our Sect. 4).

4. Hydrodynamical modelling

We aimed to infer the progenitor and CSM properties by comparing the bolometric LC and velocity evolution to models computed using the one-dimensional Lagrangian local thermodynamic equilibrium radiation hydrodynamics code from Bersten et al. (2011). Given that moderate CSM structures do not

Table 4. Properties of the pre-SN model grid calculated by Nomoto & Hashimoto (1988) used in this work.

Model	M_{ZAMS}	$M_{\mathrm{pre-SN}}$	$R_{\mathrm{pre-SN}}$	M_{core}	M_{H}	M_{ej}
M13	13	12.73	576	1.6	6.17	11.13
M15	15	14.11	517	1.7	6.77	12.41
M18	18	16.74	729	1.7	7.51	15.04
M20	20	18.35	812	1.8	7.93	16.55
M25	25	21.69	1234	2.0	8.44	19.69

Notes. From left to right: model name, ZAMS mass (M_{ZAMS}), pre-SN mass ($M_{\mathrm{pre-SN}}$), pre-SN radius ($R_{\mathrm{pre-SN}}$), compact core remnant mass (M_{core}), H mass (M_{H}) and ejecta mass (M_{ej}).

significantly influence bolometric LCs of SNe II at times $\gtrsim 30$ d (Morozova et al. 2018; Martinez et al. 2022b), it is practical to divide the SN 2024ggi modelling into two steps.

In Sect. 4.1 we focus on inferring the global parameters such as the explosion energy (E_{exp}), the progenitor mass and radius, and the nickel mass ($M_{^{56}\mathrm{Ni}}$) and its mixing (mix(^{56}Ni)[3]) by matching the plateau luminosity and duration, as well as the Fe II line velocities with our models. In Sect. 4.2 we then focus on deriving the CSM parameters such as the CSM extension (R_{CSM}) and mass-loss rate ($\dot{M}$) for different wind prescriptions (steady and accelerated). The CSM was artificially included in the outermost regions of our progenitor models. We then matched the cooling phase luminosity, duration, and steepness, as well as the line velocities, with our models. In this work, we adopted a cooling phase duration of $Cd = 26$ d, derived from the bolometric LC (see Sect. 3.3), to distinguish the CSM interaction-dominated phase from the rest of the evolution. Lastly, a complete model was calculated using the parameter set derived from the two-step modelling.

4.1. Global parameter modelling

Our hydrodynamical code requires progenitor models at the time of core collapse in order to initialise the explosion. For this work we utilised a pre-SN model grid calculated by Nomoto & Hashimoto (1988), which comprises a RSG set with ZAMS masses of 13, 15, 18, 20, and 25 $M_\odot$. For simplicity, we refer to these progenitor models by their ZAMS masses prefixed with the letter M (e.g. M13). The main properties of our pre-SN models are listed in Table 4. The explosion is then simulated by depositing some energy in the form of a thermal bomb at a mass coordinate where the pre-SN structure is assumed to collapse into a compact remnant (M_{core}), and is thus removed from our calculations.

A set of hydrodynamical models was generated by varying several physical parameters for each of our pre-SN models. We explored different values of E_{exp} in the range $0.5-1.7$ foe (1 foe = 10^{51} erg), $M_{^{56}\mathrm{Ni}}$ in the range $0.01-0.06\,M_\odot$ and mix(^{56}Ni) in the range 10–80%. Then, we visually compared the model set with the bolometric LC and Fe II line velocities of SN 2024ggi derived in Sects. 3.2 and 3.3 to select our preferred model.

To choose an adequate progenitor model, we used the well-known fact that for a given pre-SN model (with a fixed mass and radius), E_{exp} is the only parameter that can mod-

---

[3] The ^{56}Ni mixing is defined as the percentage of the total pre-SN mass to which the ^{56}Ni is uniformly distributed.

ify the ejecta expansion velocities (Kasen & Woosley 2009; Dessart et al. 2013; Bersten 2013). Thus, our initial exploration focused on finding appropriate E_{exp} values to reproduce the Fe II velocities of SN 2024ggi across our pre-SN model grid. From this analysis, we find that only the M13, M15, and M18 models could reproduce the Fe II line velocities using E_{exp} values of 1.5, 1.2, and 1.7 foe, respectively, and also provide a reasonable LC of SN 2024ggi. For more massive models, no solution was found.

Subsequently, we focused on refining the bolometric LC match through an exploration of the nickel mass and distribution ($M_{^{56}\mathrm{Ni}}$ and mix(^{56}Ni)), the remaining free parameters available. From this exploration we find that M15 models provide an overall better agreement with the observations of SN 2024ggi.

In Fig. 3 we present our preferred solution, which corresponds to the M15 model with an explosion energy of $E_{\mathrm{exp}} = 1.2$ foe and a ^{56}Ni mass of $M_{^{56}\mathrm{Ni}} = 0.035\,M_\odot$ with mix(^{56}Ni) = 30%. We also present two additional models, M13 (dashed green line) and M18 (dashed pink line), as a comparison. Although these models provide a comparable match to the Fe II velocities as our preferred M15 model, the same is not true for the LC of SN 2024ggi. As can be seen in Fig. 3, both models have a steeper plateau decline rate than what is observed, overestimate the plateau luminosity early on, and produce a shorter (M13) or longer (M18) plateau duration. Therefore, these models produce a poorer match to the data than our preferred M15 model. However, we cannot rule out some intermediate models from our analysis.

The M15 model provides a good representation of the plateau, the transition, and the onset of the radioactive tail. However, we posit that the derived nickel properties should be taken with caution due to the relatively large uncertainties starting at $t \sim 87$ d, combined with the lack of observations beyond $t \sim 124$ d after the explosion. Nevertheless, given the strong correlation between radioactive tail luminosity and ^{56}Ni mass (Martinez et al. 2022c), it is possible to rule out values of $M_{^{56}\mathrm{Ni}} \gtrsim 0.035\,M_\odot$, as they produce radioactive tail luminosities exceeding the faintest observed transition luminosity. We also note that our choice of progenitor and E_{exp} parameters is not altered by the exploration of nickel parameters, as these do not affect the expansion velocities and have a comparatively small influence on the plateau characteristics.

From our exploration, we conclude that the M15 model with an explosion energy of $E_{\mathrm{exp}} = 1.2$ foe, a ^{56}Ni mass of $M_{^{56}\mathrm{Ni}} = 0.035\,M_\odot$ with mix(^{56}Ni) = 30% is a model that closely represents the Fe II velocities and the bolometric LC of SN 2024ggi at times $t \gtrsim 26$ d. This model is presented in Fig. 3. Although our analysis is based on visual comparisons, we deem our choice of the optimal physical parameters to be well justified within the assumptions of our modelling. A more refined statistical analysis is beyond the scope of this study.

4.2. CSM parameter modelling

The models presented in Sect. 4.1 fail to reproduce the early observations since they underestimate the bolometric luminosity up to $t \sim 26$ d. This discrepancy has been attributed to the effect of the interaction between the ejecta and an existing CSM. It has been established that the incorporation of a CSM distribution at the outermost layers of the pre-SN structure increases the luminosity of the resulting model during the cooling phase, thus improving the early-time modelling (Moriya et al. 2011;

Morozova et al. 2018; Englert Urrutia et al. 2020). The presence of CSM also lowers the maximum photospheric velocity and halts the velocity decline during the cooling phase, which can help constrain the plausible CSM configurations. The existence of a CSM structure in SN 2024ggi is further supported by the presence of flash features in the early-time spectra (Hoogendam et al. 2024; Jacobson-Galán et al. 2024; Pessi et al. 2024; Chen et al. 2024; Shrestha et al. 2024).

On that basis, we modified the density profile of the M15 progenitor model by attaching a CSM distribution before simulating the explosion. We used the same explosion parameters as those of our preferred model presented in Sect. 4.1. Only the CSM properties are explored, which mainly affect the LC and expansion velocities for $t \lesssim 26$ d. We note that different CSM configurations introduce slight variations during the transition to the radioactive tail. However, these differences are too small to warrant a re-evaluation of the model parameters derived in Sect. 4.1.

In this section we present two different scenarios: a steady wind distribution ($\rho \propto r^{-2}$) and an accelerated wind distribution. In both cases, a set of models was explored and visually compared with the SN 2024ggi data. In the following, we present and discuss the best models found within our exploration. However, it must be noted that we cannot rule out other possible solutions given the qualitative nature of our analysis and the well-known degeneracies between CSM parameters (Dessart & Jacobson-Galán 2023; Khatami & Kasen 2024). To refine the parameter exploration, a statistical study with a broader parameter grid needs to be performed, which is left for future work.

For the steady wind scenario, the wind velocity was fixed at $v_w = 77$ km s^{-1}, as measured by Pessi et al. (2024), and different CSM extensions and mass-loss rates were explored. Note that Shrestha et al. (2024) measured a $v_w = 37$ km s^{-1} from the full width at half maximum (FWHM) of the Hα line. However, the FWHM corresponds to v_w only in the optically thin case, which might not be the case for 2024ggi at the epoch when those measurements were made. We used the measurements from the narrow component of Hα assuming that an optically thick CSM is a better proxy for v_w.

The preferred steady-wind model is shown in Fig. 3, and it greatly improves the early LC and expansion velocities modelling as a result of the inclusion of this CSM. Said model has an extension of $R_{CSM} = 1200 R_\odot$ and a mass-loss rate of $\dot{M} = 3.6 M_\odot$ yr^{-1}, corresponding to a CSM mass of $M_{CSM} = 0.7 M_\odot$. The inferred mass-loss rate is considerably higher than the typical range for SNe II-P, suggesting an enhanced mass loss event during the last ~ 70 d before the explosion (Morozova et al. 2017).

We also examined whether this model was able to reproduce the duration of the flash features in the observed spectra. Following Dessart et al. (2017), the narrow lines last as long as the shock is placed within a slow-moving optically thick material (i.e. until the shock goes through the SN photosphere). In our model we find that the flash features should disappear ~ 0.1 d after shock breakout. This duration is an order of magnitude lower than the estimated value of 3.8 ± 1.6 d for SN 2024ggi (Jacobson-Galán et al. 2024) and could be a plausible reason to consider the steady wind model less favourably.

For the accelerated wind scenario, we followed the wind velocity prescription given by Moriya et al. (2018), which takes the form of the β velocity law given below:

$$v_w(r) = v_0 + (v_\infty - v_0)(1 - R_0/r)^\beta, \qquad (1)$$

where v_0 is the initial wind velocity (0.1 km s^{-1}), v_∞ is the terminal wind velocity (77 km s^{-1}, Pessi et al. 2024), R_0 is the radial coordinate where the CSM is attached to the progenitor model, and β is the wind acceleration parameter (Lamers & Cassinelli 1999).

We then explored different CSM extensions, mass-loss rates and wind acceleration parameters, and compared the resulting model grid with the early-time bolometric LC and line velocities. The preferred accelerated wind model has an extension of $R_{CSM} = 3000 R_\odot$, a mass-loss rate of $\dot{M} = 4.6 \times 10^{-3} M_\odot$ yr^{-1} and a wind acceleration parameter of $\beta = 9$, corresponding to a CSM mass of $M_{CSM} = 0.55 M_\odot$. This model, shown in Fig. 3, greatly improves the modelling of early-time observations compared to the CSM-free model. It produces a bolometric LC similar to the steady wind model, albeit more luminous and with a steeper decline rate during the first ~ 15 d of evolution. Likewise, the photospheric velocity evolutions of the two CSM models are comparable, although the accelerated wind model yields slightly lower velocities during the first ~ 15 d. Since Fe II velocity measurements before t $\lesssim 15$ d are lacking, we cannot further constrain the CSM properties of SN 2024ggi. Nevertheless, the maximum ejecta velocity during the first ~ 15 d of all our models never exceeds 9000 km s^{-1}, which is in agreement with the results by Hu et al. (2025), where the shock velocity is reported to be approximately 10 000 km s^{-1}.

We note that the optimal wind acceleration parameter found in our exploration is higher than the typical range for normal RSGs (1–5, Moriya et al. 2018). This would be consistent with an enhanced mass-loss event scenario prior to the explosion. We also examined the duration of the flash features, and found that they should last for ~2.4 d after shock breakout. This is an improvement over the relatively short-lived prediction in our preferred steady wind model, and closer to, though still shorter than the estimated duration in SN 2024ggi (3.8 ± 1.6 d, Jacobson-Galán et al. 2024).

Despite the accelerated wind scenario producing a $\dot{M}$ value three orders of magnitude lower than the steady wind model, the total M_{CSM} remains roughly similar in the two cases. This consistency in the inferred M_{CSM} is noteworthy, as it suggests that a similar amount of material was needed in both scenarios to decelerate the shock wave and thereby produce lower expansion velocities. On the other hand, the mass-loss rate is associated with the late evolutionary history of the progenitor star, and thus remains largely unconstrained despite recent efforts (Quataert & Shiode 2012; Woosley & Heger 2015; Fuller & Tsuna 2024).

The density profiles of the steady and accelerated wind models are shown in the inset of Fig. 3. The two CSM profiles exhibit similar density and steepness up to a radius of $R \simeq 1000 R_\odot$, indicating the presence of a dense and compact CSM core. Beyond this extension, in the range of $R \simeq 1000-3000 R_\odot$, the accelerated wind model shows a sharp drop in density forming a low-density tail. This configuration – an inner dense and compact core coupled with an outer light and extended tail – resembles the two-component CSM distribution proposed in recent studies (Chugai & Utrobin 2022; Jacobson-Galán et al. 2023; Hu et al. 2025; Zimmerman et al. 2024). The two-component CSM models offer a promising pathway to explain the CSM mass required to reproduce the early-time bolometric LC while providing more realistic mass-loss scenarios. Therefore, we consider the accelerated wind model to be the more reasonable prescription for the CSM structure of SN 2024ggi, which in turn provides a more credible timescale for the duration of the flash features as discussed above.

5. Conclusions

In this work we present optical photometric and spectroscopic observations of the Type II SN 2024ggi, spanning from 2 to 106 days after the explosion. Similar to SN 2023ixf, SN 2024ggi is among the closest SNe of the decade, providing a unique opportunity to constrain the progenitor properties of SNe II. The analysis of the bolometric LC suggests that SN 2024ggi is a typical Type II SN. Nevertheless, it shows a longer plateau duration and a faster decline in the cooling phase compared to a distribution of SNe II. We have presented the first hydrodynamical modelling of the bolometric LC and photospheric velocity evolution of SN 2024ggi, using the full extent of the plateau phase. Our results suggest that SN 2024ggi originated from the explosion of a star with a ZAMS mass of $15\,M_\odot$, an explosion energy of 1.2×10^{51} erg, a ^{56}Ni production of $\lesssim 0.035\,M_\odot$, and a relatively moderate ^{56}Ni mixing of 30%. The exploded RSG star at the final stage of its evolution had a mass of $14\,M_\odot$ and a radius of $516\,R_\odot$.

To characterise the CSM around the progenitor star, we modelled the early phases of the explosion by modifying the outermost density profile and considering two different scenarios: steady winds and accelerated winds. In the steady wind case, the preferred model suggests a CSM extension of $1200\,R_\odot$ (8.3×10^{13} cm) with a mass-loss rate of $3.6\,M_\odot\,\mathrm{yr}^{-1}$, corresponding to a total CSM mass of $0.7\,M_\odot$. This model predicts a maximum flash features duration of 0.1 d. For the accelerated wind case, the preferred model points to a CSM extension of $3000\,R_\odot$ (2.1×10^{14} cm) with a mass-loss rate of $4 \times 10^{-3}\,M_\odot\,\mathrm{yr}^{-1}$ and an acceleration parameter of $\beta = 9$, resulting in a similar CSM mass of $0.55\,M_\odot$. In this case, the duration of the flash features is 2.4 d, which is closer to the observations. While both models reproduce the bolometric LC and expansion velocity evolution reasonably well, we consider the accelerated wind scenario to be more reasonable as it provides a lower mass-loss rate and a slightly better agreement with the duration of the flash features.

Several works in the literature have analysed the early properties of SN 2024ggi, which gave us something to compare our inferred parameters with. Studies modelling early spectra of SN 2024ggi found a CSM confined to a range of $R_{\mathrm{CSM}} = 2.7-5 \times 10^{14}$ cm ($3900-7200\,R_\odot$), formed from a progenitor with a mass-loss rate in the range $10^{-3}-10^{-2}\,M_\odot\,\mathrm{yr}^{-1}$ (Jacobson-Galán et al. 2024; Shrestha et al. 2024; Zhang et al. 2024b). Additionally, Chen et al. (2025) present a hydrodynamical model of the first ~ 15 days of only the LC information and find that the data are well matched by a model with an explosion energy of 2×10^{51} erg, a mass-loss rate of $10^{-3}\,M_\odot\,\mathrm{yr}^{-1}$ (assuming an accelerated wind with $\beta = 4.0$ and a terminal wind velocity of $10\,\mathrm{km\,s}^{-1}$), and a confined CSM with a radius of $R_{\mathrm{CSM}} = 6 \times 10^{14}$ cm ($\sim 8600\,R_\odot$) and a mass of $0.4\,M_\odot$. Despite the difference in methodology, our estimations of the CSM parameters, except for R_{CSM}, are in agreement with those calculated in the literature.

Studies analysing the pre-explosion data of the SN site identified a RSG star with an estimated mass ranging from 13 to $17\,M_\odot$ as a progenitor candidate of SN 2024ggi (Xiang et al. 2024; Chen et al. 2025). Furthermore, environmental studies of the SN site suggest a lower-mass progenitor, compatible with $10\,M_\odot$ (Hong et al. 2024). Our findings align with the estimates derived from direct detections. Moreover, our analysis of the morphological parameters of the bolometric LC of SN 2024ggi reveals a longer plateau compared to SN 2023ixf and a sample of SNe II from the CSP-I. This suggests that the progenitor of SN2024ggi was more massive than that of SN2023ixf and the average progenitor mass in the CSP-I sample, in line with what we find in our hydrodynamic modelling.

The recent detection of two of the closest SNe II of the decade, SN 2023ixf and SN 2024ggi, highlights the importance of early, high-cadence observations in constraining the physics of both the explosion and the progenitor stars of SNe II. Continued monitoring of SN 2024ggi during the nebular phase and after its emission fades, to confirm the disappearance of the progenitor candidate, will provide critical insights into its nature.

Data availability

The spectra presented in this paper are available via the WISeREP[4] archive (Yaron & Gal-Yam 2012).

References

Anderson, J. P., González-Gaitán, S., Hamuy, M., et al. 2014, ApJ, 786, 67
Baron, E., Branch, D., Hauschildt, P. H., et al. 2000, ApJ, 545, 444
Bersten, M. C. 2013, arXiv e-prints [arXiv:1303.0639]
Bersten, M. C., Benvenuto, O., & Hamuy, M. 2011, ApJ, 729, 61
Bersten, M. C., Orellana, M., Folatelli, G., et al. 2024, A&A, 681, L18
Brennan, S. J., & Fraser, M. 2022, A&A, 667, A62
Bruch, R. J., Gal-Yam, A., Yaron, O., et al. 2023, ApJ, 952, 119
Cardelli, J. A., Clayton, G. C., & Mathis, J. S. 1989, ApJ, 345, 245
Cartier, R., Contreras, C., Stritzinger, M., et al. 2024, A&A, submitted, [arXiv:2410.21381]
Chandra, P., Maeda, K., Nayana, A. J., et al. 2024, ATel, 16612, 1
Chen, X., Kumar, B., Er, X., et al. 2024, ApJ, 971, L2
Chen, T.-W., Yang, S., Srivastav, S., et al. 2025, ApJ, 983, 86
Chugai, N., & Utrobin, V. 2022, Astron. Lett., accepted [arXiv:2205.07749]
Chugai, N. N., Chevalier, R. A., & Utrobin, V. P. 2007, ApJ, 662, 1136
Contreras, C., Hamuy, M., Phillips, M. M., et al. 2010, AJ, 139, 519
Dessart, L., & Jacobson-Galán, W. V. 2023, A&A, 677, A105
Dessart, L., Hillier, D. J., Waldman, R., & Livne, E. 2013, MNRAS, 433, 1745
Dessart, L., Hillier, D. J., Audit, E., Livne, E., & Waldman, R. 2016, MNRAS, 458, 2094
Dessart, L., Hillier, D. J., & Audit, E. 2017, A&A, 605, A83
Elmhamdi, A., Danziger, I. J., Chugai, N., et al. 2003, MNRAS, 338, 939
Englert Urrutia, B. N., Bersten, M. C., & Cidale, L. S. 2020, Boletin de la Asociacion Argentina de Astronomia La Plata Argentina, 61B, 51
Marti-Devesa, G., & Fermi-LAT Collaboration. 2024, ATel, 16601, 1
Ferrari, L., Folatelli, G., Ertini, K., Kuncarayakti, H., & Andrews, J. E. 2024, A&A, 687, L20
Flewelling, H. A., Magnier, E. A., Chambers, K. C., et al. 2020, ApJS, 251, 7
Fuller, J., & Tsuna, D. 2024, Open J. Astrophys., 7, 47
Gutiérrez, C. P., Anderson, J. P., Hamuy, M., et al. 2014, ApJ, 786, L15
Gutiérrez, C. P., Anderson, J. P., Hamuy, M., et al. 2017, ApJ, 850, 89
Hamuy, M., Folatelli, G., Morrell, N. I., et al. 2006, PASP, 118, 2
Hillier, D. J., & Dessart, L. 2019, A&A, 631, A8
Hong, X., Sun, N.-C., Niu, Z., et al. 2024, ApJ, 977, L50
Hoogendam, W., Auchettl, K., Tucker, M., et al. 2024, TNSAN, 103, 1
Hu, M., Ao, Y., Yang, Y., et al. 2025, ApJ, 978, L27
Itagaki, K. 2023, TNSTR, 2023-1158, 1
Jacobson-Galán, W. V., Dessart, L., Margutti, R., et al. 2023, ApJ, 954, L42

---

[4] https://www.wiserep.org/

Jacobson-Galán, W. V., Davis, K. W., Kilpatrick, C. D., et al. 2024, ApJ, 972, 177
Jencson, J. E., Pearson, J., Beasor, E. R., et al. 2023, ApJ, 952, L30
Kasen, D., & Woosley, S. E. 2009, ApJ, 703, 2205
Khatami, D. K., & Kasen, D. N. 2024, ApJ, 972, 140
Killestein, T., Ackley, K., Kotak, R., et al. 2024, TNSAN, 101, 1
Kilpatrick, C. D., Foley, R. J., Jacobson-Galán, W. V., et al. 2023, ApJ, 952, L23
Kloppenborg, B. K. 2024, Observations from the AAVSO International Database, https://www.aavso.org, accessed: 2024-10-01
Komura, Y., Matsunaga, K., Uchida, H., & Enoto, T. 2024, ATel, 16595, 1
Koribalski, B. S., Staveley-Smith, L., Kilborn, V. A., et al. 2004, AJ, 128, 16
Lamers, H. J. G. L. M., & Cassinelli, J. P. 1999, Introduction to Stellar Winds (Cambridge, UK: Cambridge University Press)
Leonard, D. C., Filippenko, A. V., Gates, E. L., et al. 2002, PASP, 114, 35
Liu, C., Chen, X., Er, X., et al. 2023, ApJ, 958, L37
Lutovinov, A. A., Semena, A. N., Mereminskiy, I. A., et al. 2024, ATel, 16586, 1
Margutti, R., & Grefenstette, B. 2024, ATel, 16587, 1
Martinez, L., Bersten, M. C., Anderson, J. P., et al. 2022a, A&A, 660, A40
Martinez, L., Bersten, M. C., Anderson, J. P., et al. 2022b, A&A, 660, A41
Martinez, L., Anderson, J. P., Bersten, M. C., et al. 2022c, A&A, 660, A42
Moriya, T., Tominaga, N., Blinnikov, S. I., Baklanov, P. V., & Sorokina, E. I. 2011, MNRAS, 415, 199
Moriya, T. J., Förster, F., Yoon, S.-C., Gräfener, G., & Blinnikov, S. I. 2018, MNRAS, 476, 2840
Morozova, V., Piro, A. L., & Valenti, S. 2017, ApJ, 838, 28
Morozova, V., Piro, A. L., & Valenti, S. 2018, ApJ, 858, 15
Neustadt, J. M. M., Kochanek, C. S., & Smith, M. R. 2024, MNRAS, 527, 5366
Niu, Z., Sun, N.-C., Maund, J. R., et al. 2023, ApJ, 955, L15
Nomoto, K., & Hashimoto, M. 1988, Phys. Rep., 163, 13
Pastorello, A., Sauer, D., Taubenberger, S., et al. 2006, MNRAS, 370, 1752
Paturel, G., Teerikorpi, P., Theureau, G., et al. 2002, A&A, 389, 19
Pérez-Fournon, I., Poidevin, F., Aguado, D. S., et al. 2024, TNSAN, 107, 1
Perley, D. A., Gal-Yam, A., Irani, I., & Zimmerman, E. 2023, TNSAN, 119, 1
Pessi, T., Cartier, R., Hueichapan, E., et al. 2024, A&A, 688, L28
Poznanski, D., Prochaska, J. X., & Bloom, J. S. 2012, MNRAS, 426, 1465
Qin, Y.-J., Zhang, K., Bloom, J., et al. 2024, MNRAS, 534, 271
Quataert, E., & Shiode, J. 2012, MNRAS, 423, L92
Ryder, S., Maeda, K., Chandra, P., Alsaberi, R., & Kotak, R. 2024, ATel, 16616, 1
Schlafly, E. F., & Finkbeiner, D. P. 2011, ApJ, 737, 103
Schlegel, E. M. 1990, MNRAS, 244, 269
Schlegel, D. J., Finkbeiner, D. P., & Davis, M. 1998, ApJ, 500, 525
Shrestha, M., Bostroem, K. A., Sand, D. J., et al. 2024, ApJ, 972, L15
Soraisam, M. D., Szalai, T., Van Dyk, S. D., et al. 2023, ApJ, 957, 64
Srivastav, S., Chen, T. W., Smartt, S. J., et al. 2024, TNSAN, 100, 1
Stritzinger, M. D., Taddia, F., Burns, C. R., et al. 2018, A&A, 609, A135
Tody, D. 1986, in Instrumentation in astronomy VI, ed. D. L. Crawford, Society of Photo-Optical Instrumentation Engineers (SPIE) Conference Series, 627, 733
Tonry, J. L., Denneau, L., Heinze, A. N., et al. 2018, PASP, 130, 064505
Van Dyk, S. D., Srinivasan, S., Andrews, J. E., et al. 2024, ApJ, 968, 27
Woosley, S. E., & Heger, A. 2015, ApJ, 810, 34
Xiang, D., Mo, J., Wang, X., et al. 2024, ApJ, 969, L15
Yang, S., Chen, T. W., Stevance, H. F., et al. 2024, TNSAN, 105, 1
Yaron, O., & Gal-Yam, A. 2012, PASP, 124, 668
Yaron, O., Perley, D. A., Gal-Yam, A., et al. 2017, Nat. Phys., 13, 510
Zhai, Q., Li, L., Zhang, J., & Wang, X. 2024, TNS Classif. Rep., 2024-1031, 1
Zhang, J., Li, C. K., Cheng, H. Q., et al. 2024a, ATel, 16588, 1
Zhang, J., Dessart, L., Wang, X., et al. 2024b, ApJ, 970, L18
Zimmerman, E. A., Irani, I., Chen, P., et al. 2024, Nature, 627, 759

Appendix A: Tables

Table A.1. Optical photometry of SN 2024ggi from the HSH and JS telescopes.

MJD	B	V	R	I
60416.23229	11.968 ± 0.764	11.982 ± 0.021	11.835 ± 0.022	11.740 ± 0.033
60417.02009	12.217 ± 0.065	11.973 ± 0.044	11.832 ± 0.046	11.744 ± 0.049
60417.04254	12.197 ± 0.068	11.989 ± 0.053	11.826 ± 0.033	11.723 ± 0.045
60418.00073	12.222 ± 0.054	11.973 ± 0.088	11.820 ± 0.105	11.647 ± 0.064
60418.02609	12.233 ± 0.056	11.955 ± 0.092	11.802 ± 0.033	11.675 ± 0.038
60419.01688	12.261 ± 0.045	12.006 ± 0.051	11.776 ± 0.034	11.591 ± 0.043
60420.01423	12.316 ± 0.072	11.997 ± 0.083	11.812 ± 0.054	11.604 ± 0.066
60421.99991	12.358 ± 0.060	12.046 ± 0.056	11.797 ± 0.036	11.563 ± 0.062
60423.05799	12.367 ± 0.066	12.022 ± 0.039	11.807 ± 0.049	11.569 ± 0.042
60424.01363	12.430 ± 0.834	12.114 ± 0.464	11.844 ± 0.095	11.598 ± 0.082
60425.02442	12.401 ± 0.027	12.141 ± 0.062	11.826 ± 0.029	11.617 ± 0.070
60426.06700	12.502 ± 0.049	12.186 ± 0.040	11.886 ± 0.097	11.641 ± 0.063
60426.99785	12.540 ± 0.102	12.193 ± 0.044	11.914 ± 0.031	11.630 ± 0.076
60428.00727	12.586 ± 0.066	12.261 ± 0.066	11.929 ± 0.073	11.724 ± 0.040
60430.02084	12.626 ± 0.049	12.286 ± 0.062	11.991 ± 0.042	11.738 ± 0.045
60431.02126	12.646 ± 0.062	12.268 ± 0.084	11.973 ± 0.052	11.765 ± 0.067
60431.99448	12.741 ± 0.052	12.322 ± 0.059	11.970 ± 0.052	11.787 ± 0.033
60433.00000	12.770 ± 0.055	12.316 ± 0.022	11.996 ± 0.036	11.795 ± 0.080
60434.99879	12.854 ± 0.079	12.367 ± 0.071	12.035 ± 0.064	11.850 ± 0.039
60435.98729	12.908 ± 0.076	12.415 ± 0.054	12.055 ± 0.031	11.878 ± 0.070
60437.04790	12.887 ± 0.050	12.412 ± 0.061	12.060 ± 0.041	11.849 ± 0.056
60438.99389	13.026 ± 0.052	12.458 ± 0.038	12.065 ± 0.041	11.877 ± 0.066
60441.12399	13.189 ± 0.043	12.529 ± 0.067	12.127 ± 0.042	11.908 ± 0.044
60442.98297	13.264 ± 0.074	12.545 ± 0.060	12.161 ± 0.045	11.944 ± 0.039
60443.98952	13.280 ± 0.074	12.564 ± 0.072	12.217 ± 0.057	11.894 ± 0.094
60444.98770	13.328 ± 0.091	12.594 ± 0.077	12.170 ± 0.053	11.949 ± 0.049
60445.97769	13.367 ± 0.052	12.615 ± 0.051	12.207 ± 0.070	11.934 ± 0.058

Notes. Photometry is not corrected for Galactic nor host extinction.

Table A.2. Optical photometry of SN 2024ggi from the LCOGTN 1m telescope.

MJD	g	r	i	z
60412	13.713 ± 0.01	14.153 ± 0.012	14.213 ± 0.012	14.387 ± 0.026
60418	11.831 ± 0.018	11.988 ± 0.01	12.016 ± 0.012	12.043 ± 0.016
60421	11.865 ± 0.014	11.941 ± 0.014	11.916 ± 0.012	11.947 ± 0.015
60424	12.044 ± 0.159	12.368 ± 0.196	-	-
60427	12.119 ± 0.012	12.086 ± 0.012	12.057 ± 0.011	12.026 ± 0.014
60430	12.182 ± 0.015	12.137 ± 0.008	12.101 ± 0.010	12.079 ± 0.013
60442	-	-	12.304 ± 0.017	12.252 ± 0.018
60445	12.697 ± 0.011	12.336 ± 0.006	12.339 ± 0.006	12.278 ± 0.011
60448	12.785 ± 0.021	12.392 ± 0.027	12.343 ± 0.017	12.35 ± 0.036
60451	12.806 ± 0.019	12.377 ± 0.015	12.358 ± 0.011	12.251 ± 0.015
60454	12.848 ± 0.03	12.439 ± 0.009	12.394 ± 0.009	12.314 ± 0.017
60457	12.99 ± 0.006	12.455 ± 0.005	12.404 ± 0.006	12.329 ± 0.011
60460	13.041 ± 0.007	12.486 ± 0.005	12.425 ± 0.008	12.323 ± 0.01
60463	13.069 ± 0.009	12.486 ± 0.009	12.39 ± 0.018	12.346 ± 0.043
60466	13.088 ± 0.008	12.493 ± 0.006	12.421 ± 0.008	12.337 ± 0.014
60469	13.036 ± 0.032	12.464 ± 0.012	12.415 ± 0.012	12.384 ± 0.07
60472	13.156 ± 0.007	12.516 ± 0.005	12.431 ± 0.005	12.334 ± 0.008
60475	13.187 ± 0.01	12.541 ± 0.008	12.45 ± 0.012	12.344 ± 0.017
60477	13.21 ± 0.008	12.536 ± 0.038	12.446 ± 0.007	12.335 ± 0.011
60481	13.313 ± 0.029	12.523 ± 0.011	12.458 ± 0.009	12.341 ± 0.014
60484	13.272 ± 0.013	12.575 ± 0.011	12.455 ± 0.011	12.341 ± 0.014
60486	13.347 ± 0.006	12.591 ± 0.005	12.471 ± 0.006	12.356 ± 0.01
60489	13.384 ± 0.005	12.63 ± 0.004	12.516 ± 0.005	12.404 ± 0.009
60493	13.428 ± 0.009	12.63 ± 0.011	12.537 ± 0.015	12.336 ± 0.021
60496	13.475 ± 0.008	12.66 ± 0.007	12.549 ± 0.008	12.405 ± 0.017
60517	14.312 ± 0.01	13.178 ± 0.007	12.982 ± 0.007	12.774 ± 0.013

Notes. Photometry is not corrected for Galactic nor host extinction.